https://doi.org/10.5194/nhess-2023-5
Preprint. Discussion started: 9 February 2023

Natural Hazards and Earth System Sciences
Discussions

Spatial snowpack properties in a snow-avalanche release area: An extreme dry-slab avalanche case on Mt. Nodanishoji, Japan, in 2021

Yuta Katsuyama[1], Takafumi Katsushima[1], Satoru Adachi[2], Yukari Takeuchi[1]

[1]Tohkamachi Experimental Station, Forestry and Forest Products Research Institute, Tokamachi, 948-0013, Japan
[2]Snow and Ice Research Center, National Institute for Earth Science and Disaster Resilience, Shinjo, 996-0091, Japan

Correspondence to: Yuta katsuyama (ykatsuyama2020@affrc.go.jp)

Abstract. An extreme dry-slab snow-avalanche occurred on 10 Jan. 2021 at Mt. Nodanishoji, Gifu, Japan, during a heavy snowfall. The avalanche ran down approximately 2,800 m and caused damage to trees and infrastructures. Although this avalanche was estimated to be the second largest in Japan, physical snowpack properties and their vertical structure and spatial distribution, that caused the avalanche, were not addressed in the release area just after the avalanche fall, mainly due to unsafe and lousy weather. Based on a snow depth distribution observed by an unmanned aerial vehicle and a numerical snowpack simulation in the avalanche release area, the spatial distributions of the mechanical snowpack stability and slab mass and their temporal evolutions were estimated in this study. The procedure was validated by comparing the calculation results with the observed snowpit and spatial snow depth data. The results indicated that two heavy snowfall events, ~3 and 10 days before the avalanche onset, generated two different weak layers made of precipitation particles and associated slabs above other weak layers. The older weak layer was only generated on the northward slope due to its low temperature, whereas the newer layer was predominant over the avalanche release area. The fraction of contributions of the slabs associated with the two weak layers to the total slab mass over the calculation domain was found to be 1:2.

1 Introduction

An extreme dry-slab avalanche occurred at 2:30 a.m. (local time) on 10 Jan. 2021 at Mt. Nodanishoji, Gifu, Japan (Fig. 1) during a heavy snowfall event. The avalanche ran down approximately a horizontal distance of 2,800 m, from the elevation of 1,700 m to 710 m, and caused damage to trees and infrastructures (e.g., bridges, electronic power facilities, and radio facilities). Based on the damages, the avalanche magnitude was categorized as *size-5* in the simple index representing the magnitude from *size-1* (minimum magnitude) to *size-5* (maximum magnitude) (McClung and Schaerer, 2006). Our field survey showed that the avalanche debris was more than 2.7×10^5 tons (5.0×10^5 m^3), making it the second largest avalanche in Japan (Katsushima et al., 2021). According to an eyewitness from a local mountain guide, the release area was characterized by multiple subareas, and the slab thickness seemed to be approximately 2 m in maxima (JAN, 2021). According to a local resident, avalanches have occurred mostly every winter at Mt. Nodanishoji. However, the case on 10 Jan. 2021 was the largest in the recent half the century at least. For assessing avalanche hazard risks and formulating measures to mitigate the risks, an extreme case properly documented should be helpful information. A numerical simulation of avalanche flow is also one of the powerful tools to assess and mitigate the risks, while the simulation requires physical snowpack properties in the avalanche release area, such as snowpack quantity that potentially flow down (e.g. Christen et al., 2010; Takeuchi et al., 2011). However, the Mt. Nodanishoji avalanche is not well documented because there are always risks associated with the field surveys of avalanches, especially just after they occur, and field surveys generally require a lot of effort.

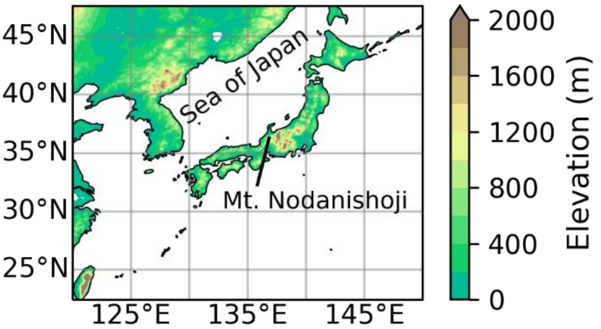

Figure 1 Location of Mt. Nodanishoji depicted with the topography of the mesoscale model (MSM).

High-magnitude avalanches have caused severe damage in many countries, but the snowpack properties in the avalanche release area are not documented frequently, similar to the Mt. Nodanishoji avalanche case. For instance, the famous *In den Arelen* avalanche, which occurred on 27 Jan. 1968 in Switzerland, was caused by a heavy snowfall that occurred 3 days before the avalanche, which destroyed some houses and killed four inhabitants (Christen et al., 2010; SLF, 1969). The avalanche ran down ~2,000 m (SLF, 1969). In Italy, the *Rigopiano* avalanche occurred by a seismic trigger on 18 Jan. 2017. The avalanche ran down ~2,200 m, caused damage to a hotel, and killed 29 people (Braun et al., 2020; Piacentini et al., 2020). Two heavy snowfall events, >10 and 0–3 days before the avalanche, made a snowpack of >3 m around the avalanche location (Calista et al., 2019; Piacentini et al., 2020). In the Pyrenees, the *Les Fonts d'Arinsal* avalanche occurred during a heavy snowfall on 8 Feb. 1996 and ran down ~1,200 m (Furdada et al., 2020). In Rogers Pass, Canada, a famous area where avalanches often occur, the maximum mass of avalanches recorded from 1909 to 1977 was estimated at 4.0×10^5 tons (Stethem et al., 2003). These past high-magnitude avalanches commonly occurred during or after heavy snowfall events. Due to bad visibility and the possibility of secondary disasters, surveying avalanche release areas just after the onset is challenging. Hence, although the snowpack structures at safe alternative locations are sometimes addressed even during bad weather, the physical snowpack properties in the release areas of high-magnitude avalanches are rarely documented. Especially in Japanese mountains, because heavy snowfall events often last a week or several weeks and the proper documents are few, snowpack properties in the avalanche release area that caused high-magnitude avalanches are poorly understood. Thus, measures mitigating the risks of high-magnitude avalanche hazards are not applied enough in Japan. A reasonable method for surveying avalanche release areas even after winter storms is necessary to understand and mitigate the hazards of high-magnitude avalanches.

The formation of dry-slab avalanches has been previously studied from the viewpoint of many factors, such as topography, wind, precipitation amount, snow grain types, and snowpack mechanical stability (Schweizer et al., 2003; Viallon-Galinier et al., 2022). Recently, many studies have developed and improved models for diagnosing the mechanical stability of snowpacks based on the sequential process concept of avalanche formation. First, a weak layer (WL) is broken progressively or rapidly by an external trigger (*failure initiation*). Second, the cracks grown from the failure location to critical lengths rapidly propagate over the slope (*crack propagation*). Finally, slabs are released if the tensile support is insufficient (*tensile failure*) (Viallon-Galinier et al., 2022). Failure initiations are traditionally diagnosed using a stability index (SI), a ratio of the snow layer strength to stress, or by an SI with the consideration of extra loadings by a human (Jamieson and Johnston, 1998). A lower value of SI indicates lower stability. Thus, the snow layers with a minimum SI across snowpack columns are the most frangible (i.e., WL). Crack propagation is diagnosed using the critical crack length (CCL): the length of a crack propagating spontaneously after failure initiation (Gaume et al., 2017; Richter et al., 2019). Tensile failure is diagnosed by a criterion derived from the ratio of the tensile strength to the maximum tensile stress of each slab layer (Reuter and Schweizer, 2018). While field experiments can diagnose the aforementioned processes, numerical snowpack models, such as SNOWPACK (Bartelt and Lehning, 2002), can also provide estimations of SI and CCL. A numerical model can be run by forcing meteorological model outputs (Quéno et al., 2016) or meteorological observations near an avalanche release area (Hirashima, 2019), although performing field surveys just after avalanche onsets is difficult due to unsafety. For instance, using the SNOWPACK model with meteorological data observed at ~2,700 m away from the release area of an avalanche by seeking the minimum SI across snowpack layers, Takeuchi et al. (2011) determined a WL made of faceted crystals (FC) and a thickness of slab accumulated over the WL that caused an extreme avalanche in Japan. Richter et al. (2021) analyzed temporal evolutions of CCLs estimated by SNOWPACK that potentially related to avalanche events during the winter season in Switzerland.

Snowpack properties are prefer to be assessed spatially, overlooking avalanche release areas. Avalanche release areas are often located in the valleys where precipitation particles (PPs) are transported from upwind and deposited by blowing snow, thus rapidly increasing snowpacks and making them mechanically unstable. Therefore, the effect of blowing snow should not be ignored when addressing the physical properties and instabilities of snowpacks for avalanches. In surveying avalanche hazards, the spatial variability is not observed due to unsafety and lots of effort, as we introduced above. Contrarily, the current numerical snowpack model does not fully treat the blowing snow effect. One may use computational tools, such as Alpine3D (Lehning et al., 2006), as they numerically simulate spatial snowpack distributions based on the blowing snow process. However, the current models do not always provide realistic snowpack distributions (Richter et al., 2021), perhaps because the topography effect on the precipitation (Houze, 2012) is not significantly considered.

Airbornes, UAVs, and satellite measurements can be used to observe the spatial distributions of snow depth even in complex terrains (Bühler et al., 2015; Eberhard et al., 2021; Goetz and Brenning, 2019). Because the observed snowpack distribution is a result of the combined effects of blowing snow and the precipitation amount affected by topography, it may bypass the numerical simulation problem for spatial snowpack distributions (Richter et al., 2021; Vögeli et al., 2016). Then, a simple calculation method was developed to obtain realistic snowpack distributions based on the combinations of the numerical snowpack model and airborne digital sensor measurements (Vögeli et al., 2016). Nevertheless, traditional mapping procedure based on airborne and UAV measurements requires ground control points (GCPs), that is challenging to install in avalanche release areas due to safety. Moreover, airborne measurements generally require high economic costs. These are barriers to applying the method of Vögeli et al. (2016) on avalanche disaster cases. However, recently, the real-time kinematic (RTK) or postprocessing kinematic (PPK) method could determine an absolute position of a UAV within an error of <10 cm. These methods have significantly improved the accuracy of snow depth measurements without the need for any GCPs (Obanawa et al., 2020).

In this study, we addressed the physical snowpack properties in the avalanche release area of Mt. Nodanishoji by a similar procedure to Vögeli et al. (2016) but using a UAV without any GCPs. We observed the snow depth distribution using a UAV in the avalanche release area 1 year after the avalanche (when we could safely perform the field survey). Then, the spatial distributions of physical snowpack properties, such as shear strength, density, and grain types, were estimated at the timing of the avalanche on 10 Jan. 2021 using the SNOWPACK model and meteorological data modified based on topography data and the observed snow depth distribution. The model calculations were evaluated by comparing them with the observed snow depth distribution and a snow pit observation near the avalanche release area.

2 Mt. Nodanishoji

Mt. Nodanishoji (elevation 1797.2 m), located at 36.2473° N 136.8523° E, is a northeastern part of the Hakusan massif around an administrative boundary between Gifu and Ishikawa prefectures, Japan (Fig. 1). The avalanche release area (upriver of Shiratani valley), approximately 1,700–1,300 m, was a ~40° slope facing eastward to northward (Fig. 2a). There was mainly no vegetation and partly shrubs on the slope (Fig. 2b). The release area is far from the nearest village and can only be reached on foot. There is much snowfall every winter, where climatological values of the precipitation amount, maximum snow depth, and air temperature were 766.8 mm, 180 cm, and 0.0°C, respectively, in December, January, and February from 1991 to 2020 at the Shirakawa site (elevation 480 m) of the Automated Meteorological Data Acquisition System (AMeDAS), the nearest meteorological observatory maintained by the Japan Meteorological Agency (JMA), approximately 5,500 m away from Mt. Nodanishoji (JMA, 2022).

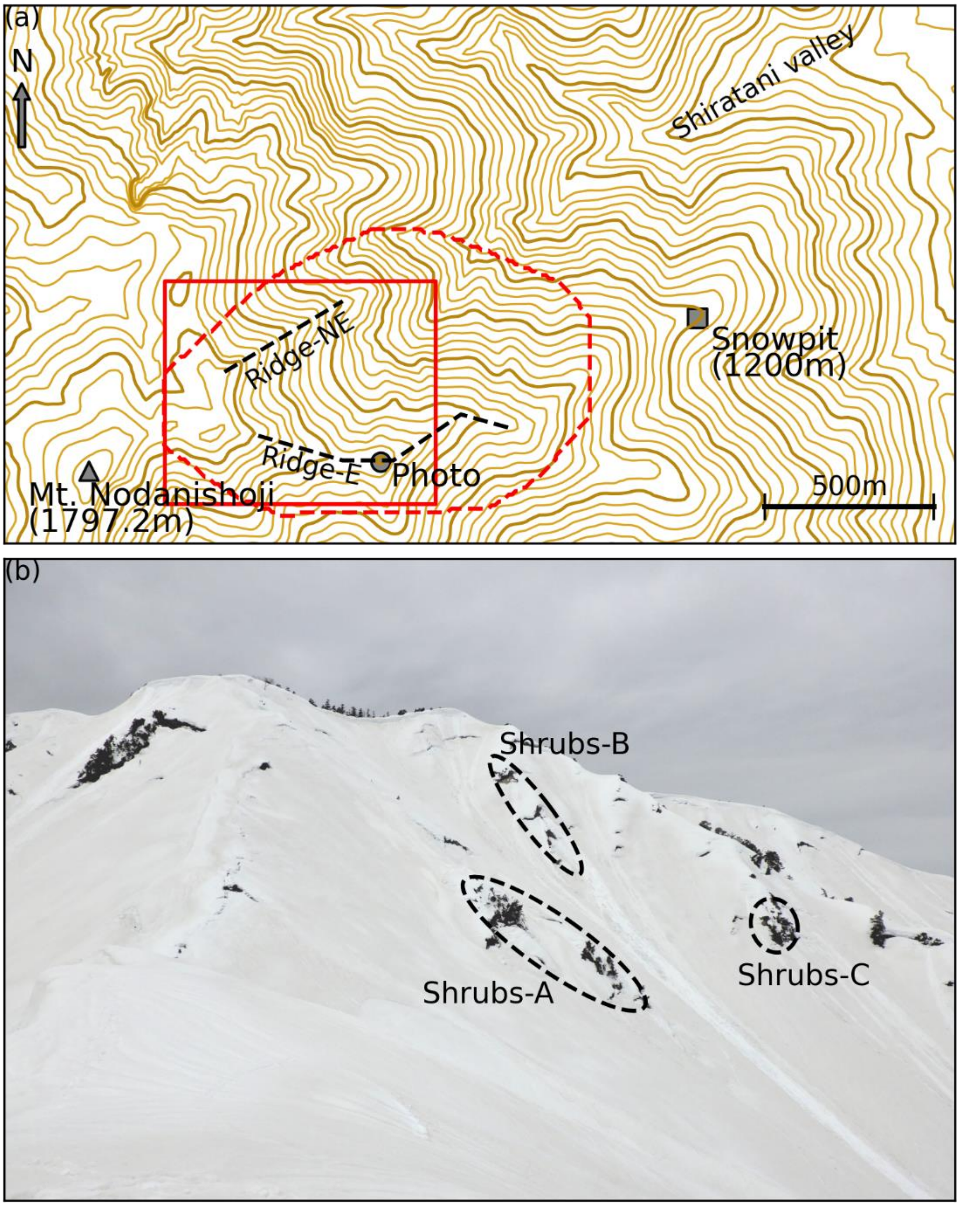

Figure 2 (a) Digital elevation model (DEM) of the 10 m spatial resolution (10-m-DEM). The thin and thick contour lines are depicted every 20 and 100 m (elevation), respectively. The peak of Mt. Nodanishoji and the snowpit observation position are indicated by a triangle and a square, respectively. The solid red square shows a calculation domain of WindNinja and the SNOWPACK model in the avalanche release area. The dashed red square shows the domain of the unmanned aerial vehicle (UAV) observation. The ridges from the western plateau of the avalanche release area to the eastward (named ridge-E) and northeastward (named ridge-NE) directions are indicated by black dashed lines. The 10-m-DEM was depicted based on data downloaded from the webpage of the Geospatial Information Authority of Japan (GSI). (b) Photo of the avalanche release area

taken from a circle marker (a) on 17 Mar. 2022. Shrubs emerged due to the snow glide (named shrubs-A, -B, and -C) and are indicated by black dashed ellipses.

3 Data and method

3.1 Field observation

The snowpit observation was performed at an elevation of 1,200 m near the avalanche release area on 24 Feb. 2022 (Fig. 2a). We selected a location as open and flat as possible as the area was forested. We manually dug the snowpit of approximately 300 cm depth. We measured the snow depth, snow water equivalent (SWE), snow grain types, and densities. The densities were measured every 10 cm using a box-cutting sampler with a thickness and volume of 3 cm and 100 cm^3, respectively. SWE was measured using a Kamuro-type snow sampler with a cross-sectional area of 20 cm^2.

The spatial distribution of the snow depth in the avalanche release area was observed on 17 Mar. 2022 by a stereo imagery measurement using a UAV (Phantom 4 RTK, DJI co.) without GCPs. In this measurement, first, 761 images were taken with 80% overwraps and 60% side overwraps between the images, 1/1000 s of exposure, auto iris, and an ISO100 sensitivity from 100 m above the ground surface. Then, a digital surface model (DSM) with 10-cm spatial resolution (10-cm-DSM) was made from the images by the Structure from Motion method using Pix4D mapper version 4.7.5. The UAV positions were determined beforehand using the PPK method with a base station, which was the nearest electronic control point of the global navigation satellite system (GNSS) maintained by the Geospatial Information Authority of Japan (GSI), approximately 5,000 m away from Mt. Nodanishoji, using RTKLIB version 2.4.2 (Takasu and Yasuda, 2009). Finally, the snow depth with 10-cm resolution was obtained by subtracting digital elevation model (DEM) with 5-m spatial resolution (5-m-DEM) measured *via* airplane laser scanning by the GSI from the DSM, after the 5-m-DEM was linearly interpolated into the same grid spacing as the 10-cm-DSM. The grid points where the snow depth exceeded 10 m or was less than 0 m were masked out as they indicated trees or were unrealistic. At the same time as the UAV observation, the snow depths at 10 points were manually measured using a snow probe to evaluate the UAV measurements. For the spatial SNOWPACK model calculation, the observed snow depth map was regridded into a grid spacing of the 5-m-DEM using a Gaussian filter with a standard deviation of 5 m. This regrid procedure filled the masked out values with surrounded grid point values.

3.2 Mesoscale model data

We used the values of the nearest grid point of the mesoscale model (MSM), an operational atmospheric model of JMA (Ishida et al., 2022), to Mt. Nodanishoji (Fig. 1) because there were no meteorological observations around the avalanche release area. The elevation of the nearest grid point was 1,081 m. The MSM data was as follows: 5-km spatial resolution and 1-h temporal interval. MSM was initialized every 3 h with a mesoscale analysis assimilated with various observation data, such as weather radar data, satellite observations, and water vapor content, from ground-based GNSS (Ikuta et al., 2021). We reconstructed hourly time series data from the initial and two leading forecast data; however, the precipitation data comprised three leading forecast data. We preliminarily checked the systematic bias of air temperature in winter by comparing the observed values at the Shirakawa AMeDAS site (elevation 480 m) and MSM values while considering the lapse temperature rate (6.5°C km^{-1}). Then, the obtained bias of ~1.7°C was subtracted from the original MSM data.

The dew point temperature, T_d (°C), which was not originally provided by the MSM, was estimated using the air temperature, T (°C), and relative humidity, f (%), based on the Tetens law. Moreover, the downward longwave radiation, $L^\downarrow$ (W m^{-2}), was estimated using the cloud fractions in the low (Q_l), middle (Q_m), and upper (Q_h) tropospheres provided by the MSM:

$$L^\downarrow = \sigma T^4 \left\{1 - \left(1 - \frac{L_f^\downarrow}{\sigma T^4}\right) C\right\}, \tag{1}$$

where σ, C, and $L_f^\downarrow$ denote the Stefan–Boltzmann constant, a factor of clouds, and the downward longwave radiation in a clear sky, respectively (Kondo et al., 1991). The cloud factor can be calculated as follows:

$$C = 0.28 \times (1 - Q)^3 - 0.82 \times (1 - Q)^2 + 1.3851 \times (1 - Q) + 0.07\ , \tag{2}$$

where Q denotes the total fraction of clouds ($= Q_l + (1 - Q_l)Q_m + \{1 - (1 - Q_l)Q_m\}Q_h$) (Kominami et al., 2012), and $L_f^\downarrow$ is calculated as follows (Kondo et al., 1991):

$$L_f^\downarrow = \{0.07(\log_{10} w_\infty)^2 + 0.19 \log_{10} w_\infty + 0.74\}\sigma T^4 \tag{3}$$

$$\log_{10} w_\infty = 0.0315 T_d - 0.1836 \tag{4}$$

3.3 Wind simulation

The surface wind distribution in the avalanche release area was estimated based on a simple numerical wind simulation using WindNinja version 3.7.2, a mass-conserving diagnostic model for simulating wind on terrain surfaces (Forthofer et al., 2014). The calculation domain of WindNinja was the same as that of the spatial SNOWPACK model (Subsection 3.4.2), which covered one of the most representative avalanche release subarea (Fig. 2a). The topography of WindNinja was configured with the 5-m-DEM, which was used to obtain the UAV snow depth (Subsection 3.1). To reduce the computational cost, in this study, we preliminarily obtained eight patterns of wind simulations calculated with a domain-averaged wind speed of 5 m s^{-1} and angles from 0° to 315° with 45° intervals (Fig. 3). Here, the wind angle was 0° for the wind from north to south and increased clockwise. Then, the wind speed at each grid point, U (m s^{-1}), was calculated as $U = U_\mathrm{m} U_\mathrm{w} / U_0$, where U_m, U_w, and U_0 denote the wind speed of MSM, the wind speed of the preliminarily obtained pattern with the closest wind angle to the MSM (Fig. 3), and the domain average wind speed for the WindNinja simulation (= 5 m s^{-1}), respectively. Note that the blowing snow effects were not considered based on the wind simulation, as the wind simulation only affected the SNOWPACK model calculations of the initial snow density and thermal energy exchanges between the atmosphere and snowpack surface (Lehning et al., 2002a).

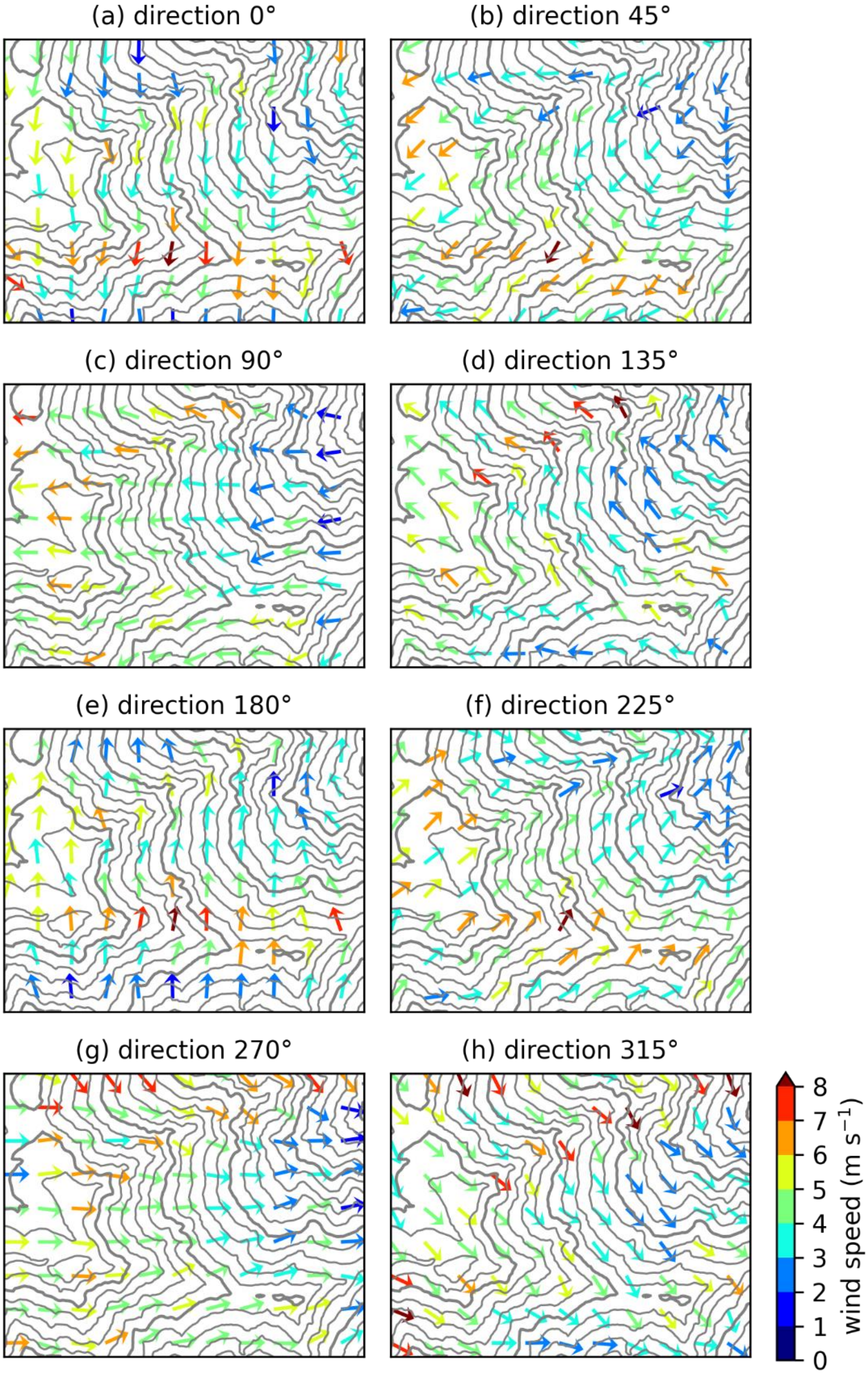
(a) direction 0°
(b) direction 45°
(c) direction 90°
(d) direction 135°
(e) direction 180°
(f) direction 225°
(g) direction 270°
(h) direction 315°
8
7
6
5
4
3
2
1
0
wind speed (m s^{-1})

Figure 3 Wind angle and speed calculated using WindNinja with a regional mean wind speed of 5 m s^{-1} and wind angles of (a) 0°, (b) 45°, (c) 90°, (d) 135°, (e) 180°, (f) 225°, (g) 270°, and 315°, respectively. The wind angle is 0° for the wind from north to south and increases clockwise. The depicted arrows were thinned out to avoid overwraps. The topography forced to WindNinja, a DEM with a 5-m spatial resolution (5-m-DEM), was depicted by thin solid contours with 20-m intervals and thick solid contours with 100-m intervals. The 5-m-DEM was downloaded from the webpage of GSI.

3.4 SNOWPACK model calculation

We used the SNOWPACK model version 3.6.0, a one-dimensional multilayered Lagrangian model that provides temporal evolutions of the physical properties of snow layers, such as layer thickness, grain type, density, temperature, and shear strength, by solving mass and energy balances (Bartelt and Lehning, 2002). The forcing meteorological variables were air temperature, precipitation, wind speed, relative humidity, downward shortwave radiation, and downward longwave radiation. The liquid precipitation fraction within the total amount, w, was determined based on the air temperature and relative humidity as follows:

$$w = \begin{cases} 1 & (T > 4 \text{ or } f > f_r) \\ 0 & (T < 0 \text{ or } f < f_s) \\ \frac{1}{2}\frac{T}{4} + \frac{1}{2}\frac{r - f_s}{f_r - f_s} & (\text{elsewhere}) \end{cases}, \tag{5}$$

where $f_s = -7.5T + 93$ and $f_r = 46\sqrt{7.2 - T}$ (Matsuo and Sasyo, 1981). The soil layers of the model were set to contain the 10 top layers of 10-cm thickness with mineral and organic soils evenly mixed, five middle layers of 20-cm thickness with mineral and organic soils evenly mixed, and a bottom layer of 8-m thickness with 100% mineral soil (Farouki, 1981; Katsuyama et al., 2020). The initial and bottom soil temperatures were given by the annual climatology of the air temperature plus 2.3°C (Hirota et al., 2002). The above model configurations for the SNOWPACK model are suitable for a wide range of Japanese snowpacks (Katsuyama et al., 2020).

We conducted two numerical experiments: one was a point simulation at the snowpit observation location at 1,200-m elevation (Subsection 3.1), and the other was a spatial simulation in the avalanche release area. In the simulation at the snowpit observation location, the air temperature, precipitation, and downward longwave radiation of the reconstructed MSM data (Subsection 3.2) were modified to compensate for the difference in the elevations between the snowpit point and MSM grid point (Subsection 3.4.1). In the spatial simulation in the avalanche release area, all the forcing variables without relative humidity were modified following the topography (Subsection 3.4.2).

3.4.1 Simulation at the snowpit observation site

The SNOWPACK model calculation was performed at the snowpit site to validate the reproducibility of the model. The calculation was started on 1 Aug. 2021 and finished at 13:00 (local time) on 24 Feb. 2022 when the snowpit observation was conducted. The MSM data without air temperature, precipitation, and downward longwave radiation was directly forced to the model. The air temperature was modified considering the standard lapse rate (6.5°C km^{-1}) between the elevation of the MSM grid point and the snowpit site. Then, the downward longwave radiation was modified by recalculating it using Eq. (1) with the modified air temperature. The precipitation was multiplied by a coefficient of 1.5, which was preliminarily obtained by comparing the mass of the observed snowpack layers and precipitation amount of the MSM corresponding to the snowpack layers (Appendix A).

3.4.2 Spatial simulation in the avalanche release area

The SNOWPACK model calculation was performed in the avalanche release area to obtain the spatial snowpack properties considering the topography and blowing snow effects. The calculation was performed by looping the SNOWPACK model at the grid points (cf. Katsuyama et al., 2020). The calculation domain, layout of the grid points, and DEM forced to the model completely matched the WindNinja calculations (Fig. 2a).

The topography and blowing snow effects were considered by modifying the input meteorological variables. The air temperature was modified by offsetting the difference of the air temperature between the grid point and MSM data expected by the difference of elevations with a lapse rate of 6.5°C km^{-1}. Calculating the shortwave radiation on the slope, the downward shortwave radiation on the flat terrain from the MSM was first divided into the beam ($I_b^{\downarrow}$) and diffuse ($I_d^{\downarrow}$) components (Reindl et al., 1990). Then, the beam component normal to the slope, I_{bs} (W m^{-2}), was simply calculated as follows:

$$I_{bs} = I_b^{\downarrow} \cos\theta_i / \cos\theta_z \,, \tag{6}$$

where θ_i and θ_z denote the solar incidence angle and solar zenith angle, respectively, whereas $I_{bs} = I_b^{\downarrow} \cos\theta_i / \cos 85°$ was in a condition of $\theta_z > 85°$ to avoid a zero division. The diffuse component on the slope, $I_{ds}^{\downarrow}$, was estimated using the model of Perez et al. (1990), who ignored a component diffused from the facing terrain. The final shortwave radiation on the slope was then the sum of I_{bs} and I_{ds}. The longwave radiation on the slope, L_s, was calculated as follows while considering a slope tilted by an angle θ_s in a celestial sphere, assuming that no radiation was emitted from the surrounding terrain and trees.

$$L_s = L^{\downarrow} (1 + \cos\theta_s)/2 \tag{7}$$

The wind speed of the MSM data was modified based on the WindNinja simulation (Subsection 3.3), and the precipitation was modified based on the result of the UAV snow depth observation:

$$P = c\, P_m H_o / \overline{H}_o, \tag{8}$$

where P_m, H_o, and $\overline{H}_o$ denote the precipitation of the MSM data, the observed snow depth distribution, and the domain average of the observed snow depth distribution, respectively (Vögeli et al., 2016). The coefficient c, which was numerically obtained as described later, was used to correct the systematic bias of the MSM precipitation.

We conducted two spatial simulations in the avalanche release area. One was a simulation in the 2021–2022 winter to obtain the coefficient c in Eq. (8) and validate the simulation by comparing it with the observed snow depth distribution, and the other was a simulation in the 2020–2021 winter to estimate the physical snowpack properties at the onset of the Mt. Nodanishoji avalanche. As for the 2021–2022 simulation, we conducted 10 simulations with the coefficient c swept from 1.0 to 1.9. Then, an optimal coefficient was obtained to be a minimum root mean square error (RMSE) for the snow depth between the simulation and UAV observation over the domain. This simulation was started on 1 Aug. 2021 and finished at noon on 17 Mar. 2022, when the UAV observation was conducted. The 2020–2021 simulation was performed from 1 Aug. 2020 to 2:00 10 Jan. 2021, just before the avalanche occurred, using the optimal coefficient c.

In the analysis for the 2020–2021 simulation, we diagnosed the snowpack mechanical stability using the classical SI, which is defined as follows:

$$S = \sigma / \rho g d \sin \theta_s \ , \qquad (9)$$

where σ, ρ, and d denote the shear strength, density, and thickness normal to the slope of each snowpack layer, respectively. g is the gravity acceleration. SI was calculated independently of each grid point and each snowpack layer. Then, WL, the most frangible snowpack layer, was defined as a layer where SI is minimum vertically across all snowpack layers at each grid point. However, WL was only defined for the grain types of the PPs, decomposing fragmented PP (DF), surface hoar (SH), FC, and depth hoar. A slab was referred to as all the layers above WL.

4 Results

4.1 Observation of snow depth distribution

Figure 4a presents the result of the UAV snow depth observation on 17 Mar. 2022. The snow depth ranged from 50 cm to 10 m in the domain and tended to be less on a plateau at the western side of the avalanche release area and along with the northern side of the ridge coming from the plateau eastward (hereafter ridge-E; Fig. 2a). Some parts at which the depth was less than 100 cm corresponded to shrubs that emerged due to snow gliding (shrubs-A, -B, and -C of Figs. 2b and 4a). The snow depth was high along with the valley and the southern side of ridge-E. In such parts, the depth was over 500 cm. The snow depth obtained by the UAV inside the avalanche release area was well consistent with the snow depth manually observed by a snow probe with less error (50 cm; Fig. 4a). However, at two of the snow probing points around a sharp ridge, the errors were over 100 cm. Note that some parts where the snow depth was over 10 m were blank because the trees were excluded by the threshold. However, regarding the data regridded into the 5-m-DEM, which was used for the SNOWPACK calculation, the blanks were filled with surrounded grid point values in applying a Gaussian filter (Subsection 3.1).

https://doi.org/10.5194/nhess-2023-5
Preprint. Discussion started: 9 February 2023

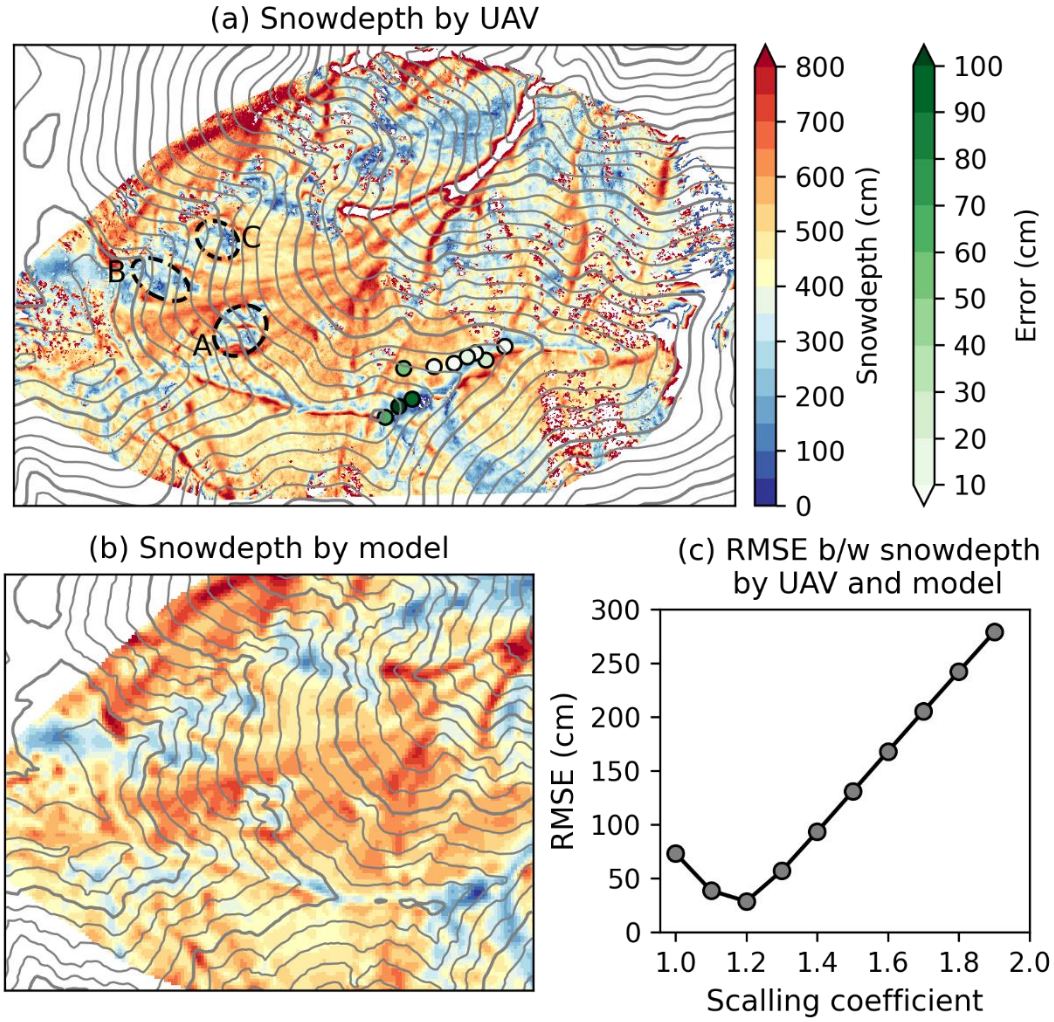

Figure 4 (a) Snow depth (shade) obtained using a UAV with a 10-cm spatial resolution and the errors (green markers) from the direct observation by a snow probe on 17 Mar. 2022. The UAV snow depth of over 10 m was masked out. The error is the difference between the snow probe observation and the average of the grid point values within 1 m from the nearest grid point to the snow probe observation. The 10-m-DEM is depicted by thin gray contours with 20-m intervals and thick gray contours with 100-m intervals. The black dashed ellipse with "A," "B," and "C" is depicted at the same locations of shrubs-A, -B, and -C, respectively (Fig. 2b). (b) Snow depth of the SNOWPACK model with a 5-m spatial resolution and a scaling coefficient of 1.2 for the precipitation amount on the same date as the UAV snow depth measurement. The 5-m-DEM is depicted by thin gray contours with 20-m intervals and thick gray contours with 100-m intervals. (c) Root mean square error (RMSE) between the snow depth of the SNOWPACK model and that of the UAV vs. the scaling coefficient for the precipitation amount. The 5-m- and 10-m-DEMs were downloaded from the webpage of GSI.

4.2 Validation of SNOWPACK model calculation

Figure 5 presents the results of the snowpit observation and SNOWPACK model calculation at 1,200-m elevation near the avalanche release area. While the calculated snow depth was ~50 cm less than the observed one, the thicknesses of PP and DF were approximately the same between the calculation and observation results. The calculated SWE of the whole snowpack was 1,526 kg m^{-2}, which was 150 kg m^{-2} less than the observation result (figure not shown). The observed vertical structures of the grain types were characterized that rounded grains (RG) were predominant below the PP and DF snowpack layers near surface (Fig. 5). This was also similar between the calculation and observation results (Fig. 5). Although a thin FC layer in the observation results was not reproduced in the calculation results on 24 Feb. 2022 (Fig. 5), the FC layer was represented at ~60 cm below the boundary between DF and RG in the calculation when the calculation was continued for one more day (figure not shown). Moreover, the observed vertical structure of the snow density was well reproduced by the model (Fig. 5).

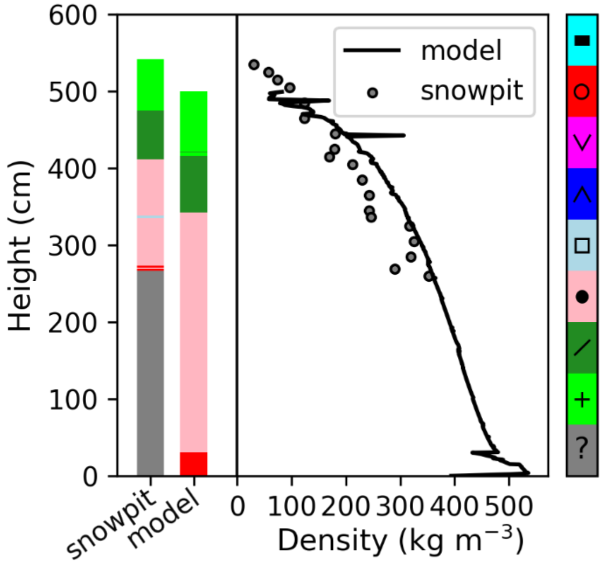

Figure 5 Snow grain types (left) and snow density (right) of the snowpit observation and the SNOWPACK model calculation at 1,200-m elevation on 24 Feb. 2022. The snow grain types are colored with a scheme of Colbeck et al. (1991), and the nonobserved layers are colored with gray.

The snow depth distribution represented by the SNOWPACK model was very similar to the observation on 17 Mar. 2022 with c = 1.2 [Eq. (8)] (Figs. 4a and b). The calculated snow depth was more than 500 cm inside the valley and on the southern side of ridge-E and ~200 cm on a plateau on the western side of the avalanche release area. The snow depth around the shrubs and glide cracks was 250–350 cm (Fig. 4b), ~50 cm more than the observation values (Fig. 4a), as snow gliding was not considered in the calculation. The errors were ~±15%, that were relatively large, on the northern side of the ridge from the plateau to the northeastward (hereafter ridge-NE; Fig. 2a) and southern sides of ridge-E (Fig. 6). The RMSE of the snow depth represented by the model was 30 cm over the calculation domain with c = 1.2 (Fig. 4c). We adopted this coefficient for the calculation presented in Subsection 4.4 because the RMSE was minimum with the coefficient (Fig. 4c).

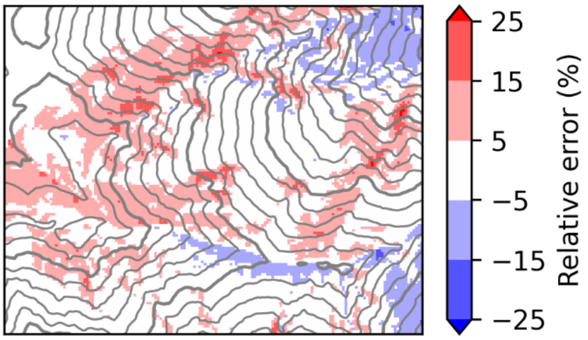

Figure 6 Relative error of the simulated snow depth by the SNOWPACK model with respect to the observed snow depth by the UAV. The 5-m-DEM, downloaded from the webpage of GSI, is depicted by thin gray contours with 20-m intervals and thick gray contours with 100-m intervals.

4.3 Meteorology in the 2020–2021 winter

Before discussing the results of the spatial snowpack distribution of the avalanche of 10 Jan. 2021, the meteorological conditions prior to the avalanche were briefly checked. The time series of the MSM data at the nearest grid point to Mt. Nodanishoji showed intermittent snowfalls from 13 Dec. 2020 (Fig. 7). There were three heavy snowfall events, which exceeded 40 mm per day, approximately every 10 days. The total precipitation amount for 3 days before the avalanche onset was 132 mm. The air temperature tended to be low during snowfall events. While the temperature was above 0°C until 11 days before the avalanche, after that, it decreased and was kept below 0°C.

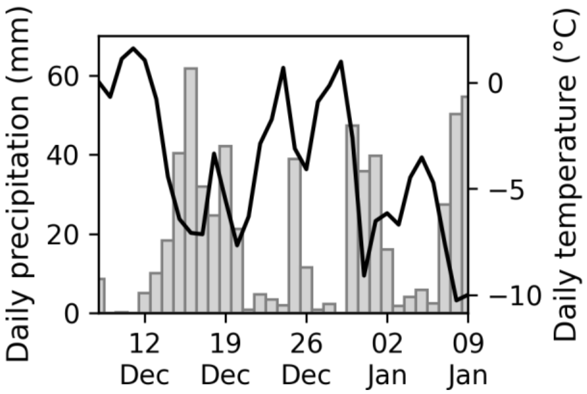

Figure 7 Daily precipitation (bar) and daily mean air temperature (solid line) at the nearest grid point of MSM to Mt. Nodanishoji from 8 Dec. 2020 to 9 Jan. 2021, a day before the avalanche onset.

4.4 Physical properties in the avalanche release area

Figures 8 and 9 present the results of the spatial SNOWPACK model calculation in the avalanche release area just before the avalanche on 10 Jan. 2021. The SIs of the WLs were less than 1.0 all over the calculation domain without on a plateau on the western side of the avalanche release area (Fig. 8a). Thus, the snowpack was significantly mechanically unstable everywhere. The grain types corresponding to the WLs were PP mostly everywhere (Fig. 8b). Tracing back to the initial depositions of these WLs, the WLs that originated from the snowfall event 0–5 days before the avalanche were predominant in most of the avalanche release area (Fig. 8c) (WL-A hereafter). Interestingly, on the northward slope, WLs originated from the snowfalls 8–12 days before the avalanche (Fig. 8c) (WL-B hereafter).

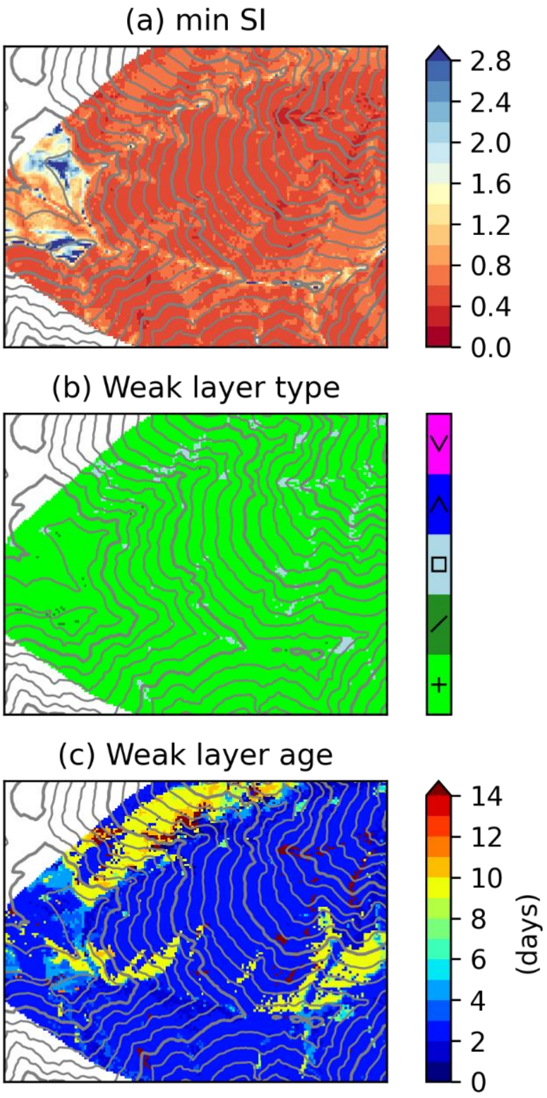

Figure 8 (a) Minimum stability index (SI) across the snow layers, (b) snow grain type of the weak layer (WL) defined as the layer whose SI is minimum, and (c) elapsed number of days (age) of the WL from the layer deposition. The 5-m-DEM, downloaded from the webpage of GSI, is depicted by thin gray contours with 20-m intervals and thick gray contours with 100-m intervals.

The spatial distribution of the WLs with the two different origins caused spatial variations in the slab thickness and density (Fig. 9). The slab thickness normal to the slope above WL-A was ~150 cm in the center of the avalanche release area and ~50 cm on the northern side of the ridge-E and around the shrubs-A, -B, and -C. This spatial distribution was basically correlated with the spatial distribution of the snow depth (Figs. 4a and 9a). The density of these slabs was ~150 kg m^{-3} (Fig. 9b). However, the slab thickness above WL-B (Fig. 8c) was ~150 cm in mean and ~200 cm in maxima with a density of 180 kg m^{-3} (Fig. 9). Hence, these old slabs were much thicker and denser than the slabs associated with the WL-A, which was deposited 0–5 days before the avalanche.

350

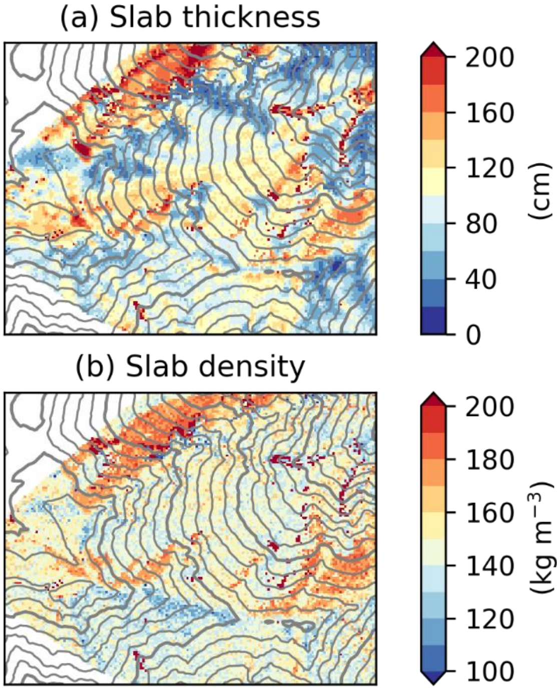

Figure 9 (a) Slab thickness above the WL and (b) slab density. The 5-m-DEM, downloaded from the webpage of GSI, is depicted by thin gray contours with 20-m intervals and thick gray contours with 100-m intervals.

355 Figure 10a presents the time evolutions of SI and temperature, averaged over the grid points where the WL ages were 0–5 days at the avalanche onset (i.e. grid points corresponding to WL-A), for the snow layers made by the snowfall 0–5 and 8–12 days before the avalanche. The SI of the newer layers was ~5.5 two days after the initial deposition, and it dropped down to ~1.0 just two days before the avalanche onset (solid green line of Fig. 10a). However, the SI of the older layers was ~1.0 nine days before the avalanche, and it gradually increased up to 2.0 three days before the avalanche. Then, it again gradually 360 decreased down to 1.5 at the avalanche onset (solid gray line of Fig. 10a) but was more than the SI of the new layers (solid green line of Fig. 10a). The temperature of these older layers was steadily increasing from −13°C nine days before the avalanche to −9°C at the avalanche onset (gray dashed line of Fig. 10a).

https://doi.org/10.5194/nhess-2023-5
Preprint. Discussion started: 9 February 2023

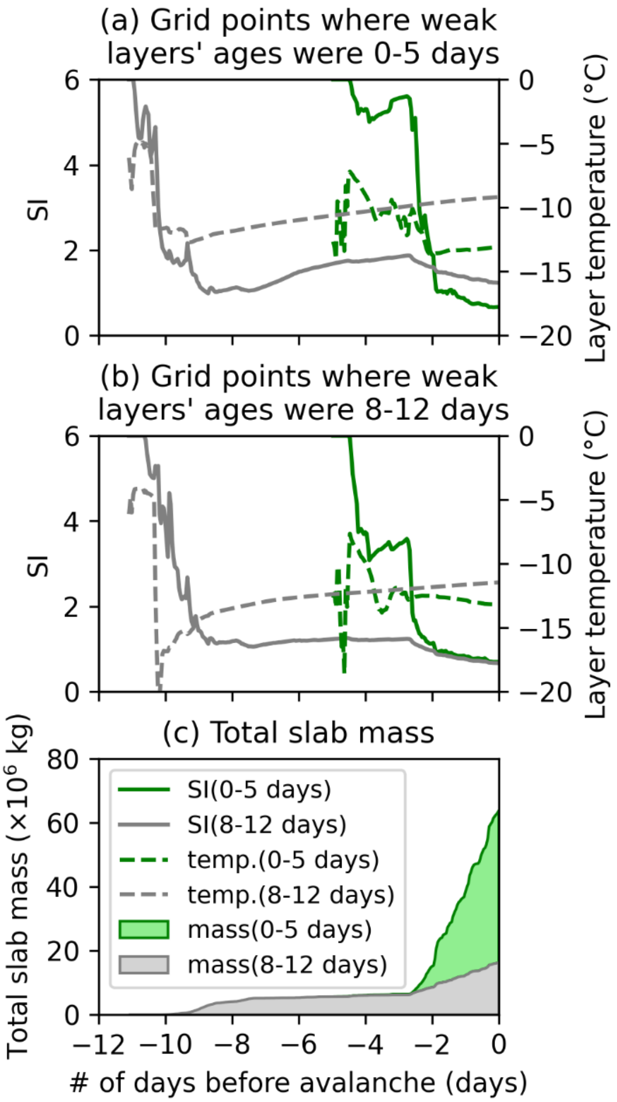

Figure 10 (a) Time evolutions of the mean SI (solid line) and mean temperature (dashed line) prior to the avalanche onset for the snow layer (green line) made by the snowfall 0–5 days before the avalanche and the layer (gray line) made by the snowfall 8–12 days before the avalanche in the grid points where WL-A was the most frangible at the avalanche onset. (b) Same as (a) but the time evolutions in the grid points where WL-B was the most frangible at the avalanche onset. (c) A stacked graph of the total slab mass above (green) WL-A and (gray) WL-B integrated over the calculation domain.

Figure 10b presents the time evolutions of SI and temperature, averaged over the grid points where the WL ages were 8–12 days at the avalanche onset (i.e. grid points corresponding to WL-B), for the snow layers made by the snowfall 0–5 and 8–12 days before the avalanche. The SI of the older layers was approximately steady at ~1.0 from nine days before the avalanche until the timing of the avalanche onset (gray solid line in Fig. 10b), which is slightly less than the SI of the newer layers (green solid line in Fig. 10b). The temperature of the older layers had been increasing from −15°C to −11°C starting from nine days before the avalanche until the avalanche onset (gray dashed line of Fig. 10b). These temperatures were 2°C colder than the temperatures of the layers originated 8–12 days before the avalanche at the grid points corresponding to WL-A (gray dashed line of Fig. 10a).

The total mass of the slabs integrated over the calculation domain began increasing rapidly three days before the avalanche onset (Fig. 10c), as there was heavy snowfall (Fig. 7) and because WL-A was predominant over the avalanche release area (Fig. 8c). Then, at the avalanche onset, the total mass reached ~60×10^6 kg with a fraction of 1:2 between the slab mass corresponding to WL-A and -B. Interestingly, even though WL-A was quite predominant in the calculation domain (Fig. 8c), the slabs corresponding to WL-B enough contributed to the total mass (Fig. 10c) as the slabs for WL-B were thicker and made of older snow than the slabs for WL-A (Fig. 9a).

5 Discussion

This study addressed the spatial distribution of the physical snowpack properties in the avalanche release area of the Mt. Nodanishoji avalanche on 10 Jan. 2021 through the combined use of UAV snow depth observations and the SNOWPACK model. This was the first case to estimate the spatial snowpack properties that caused the high-magnitude avalanche. The numerical simulation reproduced two different WLs initially deposited at 0–5 and 8–12 days before the avalanche onset, i.e., WL-A and WL-B. The slab thickness normal to the slope ranged from 50 to 200 cm, which is in line with the eyewitness of a local mountain guide. Even though the WL-B's coverage of the whole avalanche release area was much less, the slabs corresponding to WL-B occupied 1/3 of the total slab mass over the release area. Therefore, the two heavy snowfall events that occurred approximately ten and three days before the avalanche produced the potential slab mass that caused the avalanche. Moreover, considering the total slab mass released, the spatial extent of the WL failure propagation should be of secondary importance. According to an elastic theory, if the slab density was denser than 150 kg m^{-3}, the failure would propagate up to a potential maximum of the avalanche release area topographically expected (Gaume et al., 2015). In the case of the Mt. Nodanishoji avalanche, the slab would be denser than 150 kg m^{-3} over the avalanche release area. Thus, the slabs would be fully released, which was consistent with the eyewitness of the local mountain guide that the total release area almost fully consisted of subcatchments between ridge-E and ridge-NE (JAN, 2021). The obtained findings above would be valuable for administrators of the avalanche region for preventing disasters and alerting citizens. Moreover, the findings can apply to an initial condition for a numerical simulation of avalanche flow (cf. Christen et al., 2010; Takeuchi et al., 2011).

Interestingly, WL-B was only on the northern side of the slope (Fig. 8c), which was not correlated with the spatial distribution of the snowfall amounts (Fig. 4a). Based on the time evolution analysis of the snow layer temperatures, the temperatures of the layers initially deposited by the snowfall event 8–12 days before the avalanche in the northward slope were warmer by 2°C than those in the other slope aspect (Figs. 10a and b), which would cause differences in viscosity, density, and strength. For example, the viscosity of the layer at −13°C would be 25% lower than that at −15°C with a density

https://doi.org/10.5194/nhess-2023-5
Preprint. Discussion started: 9 February 2023

of 150 kg m^{-3} (Eq. (36) of Lehning et al., 2002b). This lower viscosity made the layer denser and stronger. Hence, at the avalanche onset, the snow layer initially deposited 8–12 days before the avalanche would not be the WL in many avalanche release areas without the northward slope. The above physical process on spatial variability of PPs' WLs was different from that on FCs' WLs even though the FCs' WLs also often variate depending on the slope aspects, which is well known (e.g. Birkeland et al., 1998; Birkeland 2001; Schweizer et al., 2003).

However, the UAV partially observed the height of the shrubs rather than the snow depth due to snow gliding (Fig. 4a), which affected the SNOWPACK model calculation (Figs. 4b and 6). Even though the calculation for the 2021–2022 winter overestimated the snow depth around the shrubs compared with the observation, the calculated snow depth at the avalanche on 10 Jan. 2021 might be underestimated as there was no snow gliding at this time. Moreover, the snow depth observed by the UAV was largely overestimated around the sharp ridge (Fig. 4a) due to the insufficient spatial resolution of the DEM. In these parts, it should be noted that the SNOWPACK calculation might not provide accurate results. Moreover, the calculated snow depth on 17 Mar. 2022 was ~10% overestimated/underestimated on the northward/southward slopes (Fig. 6), as the snow on the southward slope at the time of the UAV observation slightly melted. Because the model was forced with the modified precipitation amount, assuming the amount was a total result of the blowing snow and topography effect without melting (Subsection 3.4.2), the precipitation modified using Eq. (8) would be underestimated/overestimated on the southward/northward slope. In the other parts, the calculation results should be reliable as the snow depth distribution and vertical structures of the grain types and the density were well reproduced by the model with minor errors (Figs. 4–6).

The UAV snow depth observation should be performed in winter without avalanches as the spatial distribution of snow depth is assumed to be a result of the blowing snow effect in the procedure of this study. The distribution of the snow depth after the avalanche contains history of the avalanche crown, runout path, and debris, which may affect the assumption. In this study, the flight was conducted in the following year of the target avalanche, when no high-magnitude avalanche occurred to the best of our knowledge. However, because nobody can monitor all the avalanches at Mt. Nodanishoji, there is no guarantee that avalanches did not occur at all before the UAV observation. Moreover, considering the precipitation and blowing snow effects on the slope, the wind conditions during snowfall from the initial snow cover to the UAV observation are desired to be similar to those from the initial snow cover to the avalanche onset. Fortunately, in our case, the wind speeds and directions during snowfalls were very similar between the winters of 2020–2021 and 2021–2022 (Fig. 11).

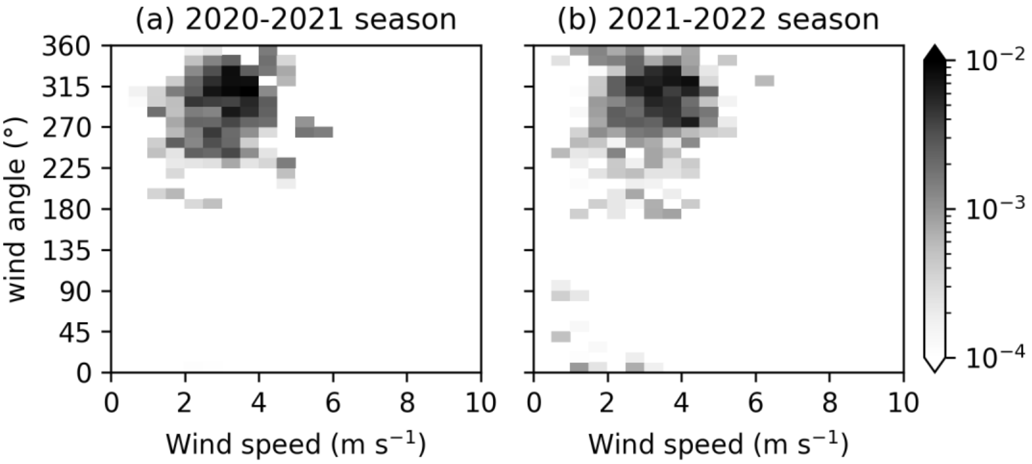

Figure 11 Joint probability distribution of the wind speed and angle weighted by the precipitation amount at the nearest grid point values of the MSM data to Mt. Nodanishoji (a) from 1 Aug. 2020 to 10 Jan. 2021 and (b) from 1 Aug. 2021 to17 Mar. 2022.

Despite the aforementioned limitations, the procedure of addressing physical snowpack properties by combining UAV snow depth observations and numerical snowpack models can be applied to other cases of high-magnitude avalanche in the future. In many snow-covered areas facing the Sea of Japan, snowfalls often occur under similar atmospheric conditions: stationary pressure pattern of the high westerly and low easterly (Takano et al., 2008). Therefore, the wind conditions during snowfalls from the initial snow cover to the timing of the UAV snow depth observation would be generally similar to those in the year of the avalanche. Moreover, the mandatory field survey was only conducted to observe the spatial snow depth distribution in the avalanche release area using the UAV once when the weather conditions were calm.

6 Conclusion

This study addressed the physical snowpack properties in the avalanche release area that caused the Mt. Nodanishoji avalanche on 10 Jan. 2021 using a UAV snow depth observation and a SNOWPACK model calculation. The results indicated that the two heavy snowfall events three and ten days before the avalanche onset generated the WLs of the PPs (i.e., WL-A and -B) that caused the avalanche. WL-B would be only on the northward slope, whereas WL-A would be majorly predominant in the avalanche release area. The temperature difference between the snow layers depending on the slope aspect would cause these two different WLs through the metamorphosis process. The fractions of the WL-A and -B contributions to the total slab mass over the domain would be 1:2. The procedure performed in this study is expected to be applied to other avalanche cases in the future due to its safety.

Appendix A: Coefficient for the precipitation correction at the snowpit site

The stratigraphy of the snow pit observation on 24 Feb. 2022 could be divided into three major layers: PP and DF of the top layers with a mass of 165 kg m^{-2}, RG between the FC and the bottom boundary of DF with a mass of 177 kg m^{-2}, and RG between the FC and upper boundary of the melt forms with a mass of 200 kg m^{-2} (Fig. 5). According to the time series of the precipitation amount at the nearest grid point of MSM to Mt. Nodanishoji, these three layers were produced by the three snowfall events with the total precipitations of 93 kg m^{-2} from 20 to 24 Feb. 2022, 131 kg m^{-2} from 15 to 20 Feb. 2022, and 144 kg m^{-2} from 1 to 15 Feb. 2022 (Fig. 7). Therefore, we used a coefficient of 1.5, which is a fraction between the total mass of the major layers and the total corresponding precipitation amount of MSM.

Data/Code availability

The DSM data observed by UAV, snow-depth data observed by a probe, and snow-pit data are available upon reasonable request to the corresponding author. SNOWPACK model code was downloaded from https://models.slf.ch/p/snowpack/downloads/. WindNinja model code was downloaded from https://github.com/firelab/windninja.

Author contribution

YK, TK, and YT designed the study. All of the authors carried out field observations. YK performed the numerical simulation. YK prepared the manuscript with contributions from all co-authors.

Competing interests

The authors declare that they have no conflict of interest.

Acknowledgments

The authors thank Dr. Yasuhiro Kominami, National Agriculture and Food Research Organization, for providing technical information to estimate longwave radiation from the MSM data. The authors also thank Mr. Ryuta Asahi, a local mountain guide, for giving us an eyewitness about the avalanche. The 5m- and 10m-DEM were provided via the download service for the basic map information by the GSI. The GNSS data for the PPK analysis was provided via the data-providing service for the electronic control point by the GSI. The numerical simulation by the SNOWPACK model was conducted using a supercomputer of AFFRIT, MAFF, Japan. YK was supported by JSPS KAKENHI (22K14458).

References

Bartelt, P., Lehning, M.: A physical SNOWPACK model for the Swiss avalanche warning Part I: numerical model, Cold Reg. Sci. Technol. 35, 123–145, doi: 10.1016/S0165-232X(02)00074-5, 2002.

Braun, T., Frigo, B., Chiaia, B., Bartelt, P., Famiani, D., Wassermann, J.: Seismic signature of the deadly snow avalanche of January 18, 2017, at Rigopiano (Italy), Sci. Rep., 10, 1–10, doi: 10.1038/s41598-020-75368-z, 2020.

Birkeland, K. W.: Spatial patterns of snow stability throughout a small mountain range, J. Glaciol. 47, 176–186, doi: 10.3189/172756501781832250, 2001.

Birkeland, K. W., Johnson, R. F., and Schmidt, D. S.: Near-Surface Faceted Crystals Formed by Diurnal Recrystallization: A Case Study of Weak Layer Formation in the Mountain Snowpack and Its Contribution to Snow Avalanches, Arctic and Alpine Research 30:2, 200–204, doi: 10.1080/00040851.1998.12002892, 1998.

Bühler, Y., Marty, M., Egli, L., Veitinger, J., Jonas, T., Thee, P., Ginzler, C.: Snow depth mapping in high-alpine catchments using digital photogrammetry, The Cryosphere., 9, 229–243, doi: 10.5194/tc-9-229-2015, 2015.

Calista, M., Miccadei, E., Piacentini, T., Sciarra, N.: Morphostructural, meteorological and seismic factors controlling landslides in weak rocks: The case studies of Castelnuovo and Ponzano (north east Abruzzo, central Italy), Geosci., 9, doi: 10.3390/geosciences9030122, 2019.

Christen, M., Bartelt, P., Kowalski, J.: Back calculation of the In den Arelen avalanche with RAMMS: Interpretation of model results, Ann. Glaciol., 51, 161–168, doi: 10.3189/172756410791386553, 2010.

Colbeck, S.C., Akitaya, E., Armstrong, R.L., Gubler, H., Lafeuille, J., Lied, K., McClung, D.M., Morris, E.M.: The international classification of seasonal snow on the ground. The International Commission on Snow and Ice of the International Association of Scientific Hydology, 23 pp., 1991.

Eberhard, L.A., Sirguey, P., Miller, A., Marty, M., Schindler, K., Stoffel, A., Bühler, Y.: Intercomparison of photogrammetric platforms for spatially continuous snow depth mapping, The Cryosphere, 15, 69–94, doi: 10.5194/tc-15-69-2021, 2021.

Farouki, O.T.: Thermal properties of soils, CRREL Mono. ed. U.S. Army Corps of Engineers, Cold Regions Research and Engineering Laboratory, Hanover, NH., 1981.

Forthofer, J.M., Butler, B.W., Wagenbrenner, N.S.: A comparison of three approaches for simulating fine-scale surface winds in support of wildland fire management. Part I. Model formulation and comparison against measurements, Int. J. Wildl. Fire, 23, 969–981, doi: 10.1071/WF12089, 2014.

Furdada, G., Margalef, A., Trapero, L., Pons, M., Areny, F., Baró, M., Reyes, A., Guinau, M.: The avalanche of les fonts d'arinsal (Andorra): An example of a pure powder, dry snow avalanche, Geosci., 10, 1–26, doi: 10.3390/geosciences10040126, 2020.

Gaume, J., Chambon, G., Eckert, N., Naaim, M., Schweizer, J.: Influence of weak layer heterogeneity and slab properties on slab tensile failure propensity and avalanche release area, The Cryosphere, 9, 795–804, doi: 10.5194/tc-9-795-2015, 2015.

Gaume, J., Van Herwijnen, A., Chambon, G., Wever, N., Schweizer, J.: Snow fracture in relation to slab avalanche release: Critical state for the onset of crack propagation, The Cryosphere, 11, 217–228, doi: 10.5194/tc-11-217-2017, 2017.

Goetz, J., Brenning, A.: Quantifying Uncertainties in Snow Depth Mapping From Structure From Motion Photogrammetry in an Alpine Area, Water Resour. Res., 55, 7772–7783, doi: 10.1029/2019WR025251, 2019.

Hirashima, H.: Numerical snowpack model simulation schemes for avalanche prediction in JapanNumerical snowpack model simulation schemes for avalanche prediction in Japan, Bull. Glaciol. Res., 37S, 31–41, doi: 10.5331/bgr.18sw02, 2019.

Hirota, T., Pomeroy, J., Granger, R.: An extension of the force restore method to estimating soil temperature at depth, evaluated for frozen soil, in sub-nival conditions, J. Geophys. Res., 107, 4767–4776, doi: 10.1029/2001JD001280, 2002.

Houze, R. A.: Orographic effects on precipitating clouds, Rev. Geophys., 50, RG1001, doi: 10.1029/2011RG000365, 2012.

Ikuta, Y., Fujita, T., Ota, Y., Honda, Y.: Variational Data Assimilation System for Operational Regional Models at Japan Meteorological Agency, J. Meteorol. Soc. Japan. Ser. II, 99, 1563–1592, doi: 10.2151/jmsj.2021-076, 2021.

Ishida, J., Aranami, K., Kawano, K., Matsubayashi, K., Kitamiura, Y., Muroi, C.: ASUCA: The JMA Operational Non-hydrostatic Model, J. Meteorol. Soc. Japan. Ser. II, 100, 825–846, doi: 10.2151/jmsj.2022-043, 2022.

Jamieson, J.B., Johnston, C.D.: Refinements to the stability index for skier-triggered dry-slab avalanches, Ann. Glaciol., 26, 296–302, doi: 10.3189/1998AoG26-1-296-302, 1998.

Japan Avalanche Network (JAN): https://snow.nadare.jp/magazines/2021/000031.html, last access: 22 June 2022.

Japan Meteorological Agency (JMA): https://www.data.jma.go.jp/obd/stats/etrn/view/nml_amd_3m.php?prec_no=52&block_no=1306&year=&month=&day=&view=, last access: 12 July 2022.

Katsushima, T., Adachi, S., Arakawa, H., Katsuyama, Y., Takeuchi, Y., Kawashima, K., 2021. Characteristics of deposition depth in dry snow slab avalanche at Mt. Nodanishoji. Proceedings of JSSI & JSSE Joint Conference on Snow and Ice Research - 2021 Chiba-Online. Chiba-Online, p. 170, doi: 10.14851/jcsir.2021.0_170, 2021 (in Japanese)

Katsuyama, Y., Inatsu, M., Shirakawa, T.: Response of snowpack to +2°C global warming in Hokkaido, Japan, J. Glaciol., 66, 83–96, doi: 10.1017/jog.2019.85, 2020.

Kominami, Y., Ohno, H., Nagata, O.: Estimating downward long-wave radiation at the surface from MSM-GPV data (2). ISAM2012. p. A-10, 2012.

Kondo, J., Nakamura, W., Yamazaki, T.: Estimation of the solar and downward atmospheric radiation, Tenki, 38, 41–48, 1991 (in Japanese).

Lehning, M., Bartelt, P., Brown, B., Fierz, C.: A physical SNOWPACK model for the Swiss avalanche warning Part III : meteorological forcing , thin layer formation and evaluation, Cold Reg. Sci. Technol., 35, 169–184, doi: 10.1016/S0165-232X(02)00072-1, 2002a.

Lehning, M., Bartelt, P., Brown, B., Fierz, C., Satyawali, P.: A physical SNOWPACK model for the Swiss avalanche warning Part II. Snow microstructure, Cold Reg. Sci. Technol., 35, 147–167, doi: 10.1016/S0165-232X(02)00073-3, 2002b.

Lehning, M., Völksch, I., Gustafsson, D., Nguyen, T.A., Stähli, M., Zappa, M.: ALPINE3D: a detailed model of mountain surface processes and its application to snow hydrology, Hydrol. Process., 20, 2111–2128, doi: 10.1002/hyp.6204, 2006.

Matsuo, T., Sasyo, Y.: Non-melting phenomena subsaturated air of snowflakes below freezing level, J. Meteorol. Soc. Japan, 59, 26–32, 1981.

McClung, D., Schaerer, P.: The avalanche handbook, 3rd ed. Mountaineers Books, 2006.

Obanawa, H., Sakanoue, S., Yagi, T.: Effectiveness of RTK-UAV measurements for estimating snow depth distribution, Trans. Japanese Geomorphol. Union, 41, 15–26, 2020 (in Japanese).

Perez, R., Ineichen, P., Seals, R., Michalsky, J., Stewart, R.: Modeling daylight availability and irradiance components from direct and global irradiance, Sol. Energy, 44, 271–289, doi: 10.1016/0038-092X(90)90055-H, 1990.

Piacentini, T., Calista, M., Crescenti, U., Miccadei, E., Sciarra, N.: Seismically induced snow avalanches: The central Italy case, Front. Earth Sci., 8, 1–27, doi: 10.3389/feart.2020.599611, 2020.

Quéno, L., Vionnet, V., Dombrowski-Etchevers, I., Lafaysse, M., Dumont, M., Karbou, F.: Snowpack modelling in the Pyrenees driven by kilometric-resolution meteorological forecasts, The Cryosphere, 10, 1571–1589, doi: 10.5194/tc-10-1571-2016, 2016.

Reindl, D.T., Beckman, W.A., Duffie, J.A.: Diffuse fraction correlations, Sol. Energy, 45, 1–7, 1990.

Reuter, B., Schweizer, J.: Describing Snow Instability by Failure Initiation, Crack Propagation, and Slab Tensile Support, Geophys. Res. Lett., 45, 7019–7027, doi: 10.1029/2018GL078069, 2018.

Richter, B., Schweizer, J., Rotach, M.W., Herwijnen, A. Van: Modeling spatially distributed snow instability at a regional scale using Alpine3D, J. Glaciol., 67, 1147–1162, doi: 10.1017/jog.2021.61, 2021.

Richter, B., Schweizer, J., Rotach, M.W., Van Herwijnen, A.: Validating modeled critical crack length for crack propagation in the snow cover model SNOWPACK, The Cryosphere, 13, 3353–3366, doi: 10.5194/tc-13-3353-2019, 2019.

Schweizer, J., Jamieson, J.B., Schneebeli, M.: Snow avalanche formation, Rev. Geophys., 41, 1016, doi: 10.1029/2002RG000123, 2003.

SLF: Schnee und Lawinen in den Schweizeralpen Winter 1967/68. Eidgenössische Drucksachen- und Materialzentrale. pp. 192, 1969.

Stethem, C., Jamieson, B., Schaerer, P., Liverman, D., Germain, D., Walker, S.: Snow avalanche hazard in Canada - A review, Nat. Hazards, 28, 487–515, doi: 10.1023/A:1022998512227, 2003.

Takano, Y., Tachibana, Y., Iwamoto, K.: Influences of Large-scale Atmospheric Circulation and Local Sea Surface Temperature on Convective Activity over the Sea of Japan in December, SOLA, 4, 113–116, doi: 10.2151/sola.2008-029, 2008.

Takasu, T., Yasuda, A.: Development of the low-cost RTK-GPS receiver with an open source program package RTKLIB. International Symposium on GPS/GNSS. Jeju, Korea, 2009.

Takeuchi, Y., Torita, H., Nishimura, K., Hirashima, H.: Study of a large-scale dry slab avalanche and the extent of damage to a cedar forest in the Makunosawa valley, Myoko, Japan, Ann. Glaciol., 52, 119–128, doi: 10.3189/172756411797252059, 2011.

Viallon-Galinier, L., Hagenmuller, P., Reuter, B., Eckert, N.: Modelling snowpack stability from simulated snow stratigraphy: Summary and implementation examples, Cold Reg. Sci. Technol., 201, 103596, doi: 10.1016/j.coldregions.2022.103596, 2022.

Vögeli, C., Lehning, M., Wever, N., Bavay, M.: Scaling Precipitation Input to Spatially Distributed Hydrological Models by Measured Snow Distribution, Front. Earth Sci., 4, doi: 10.3389/feart.2016.00108, 2016.